



# CoCrMo cellular structures made by Electron Beam Melting studied by local tomography and finite element modelling

Clémence Petit, Éric Maire, Sylvain Meille, Jérôme Adrien, Shingo Kurosu, Akihiko Chiba

## ► To cite this version:

Clémence Petit, Éric Maire, Sylvain Meille, Jérôme Adrien, Shingo Kurosu, et al.. CoCrMo cellular structures made by Electron Beam Melting studied by local tomography and finite element modelling. Materials Characterization, 2016, 116, pp.48-54. 10.1016/j.matchar.2016.04.006 . hal-02475338

**HAL Id: hal-02475338**

**<https://hal.science/hal-02475338>**

Submitted on 9 Feb 2021

**HAL** is a multi-disciplinary open access archive for the deposit and dissemination of scientific research documents, whether they are published or not. The documents may come from teaching and research institutions in France or abroad, or from public or private research centers.

L'archive ouverte pluridisciplinaire **HAL**, est destinée au dépôt et à la diffusion de documents scientifiques de niveau recherche, publiés ou non, émanant des établissements d'enseignement et de recherche français ou étrangers, des laboratoires publics ou privés.

# **CoCrMo cellular structures made by Electron Beam Melting studied by local tomography and finite element modelling**

Clémence Petit<sup>1</sup>, Eric Maire<sup>1</sup>, Sylvain Meille<sup>1</sup>, Jérôme Adrien<sup>1</sup>, Shingo Kurosu<sup>2</sup>, Akihiko Chiba<sup>2</sup>

<sup>1</sup>INSA de Lyon, MATEIS CNRS UMR5510

Université de Lyon

69621 VILLEURBANNE, France

<sup>2</sup>Institute for Materials Research

Tohoku University

Sendai 980-0812, Japan

Corresponding author: Eric Maire,

phone: +33 4 72 43 88 61

fax: +33 4 72 43 85 39

[eric.maire@insa-lyon.fr](mailto:eric.maire@insa-lyon.fr)

Keywords: Porous samples, X-ray Tomography, Mechanical behaviour, Finite Element

## **Abstract**

The work focuses on the structural and mechanical characterization of Co-Cr-Mo cellular samples with cubic pore structure made by Electron Beam Melting (EBM). X-ray tomography was used to characterize the architecture of the sample. High resolution images were also obtained thanks to local

tomography in which the specimen is placed close to the X-ray source. These images enabled to observe some defects due to the fabrication process: small pores in the solid phase, partially melted particles attached to the surface. Then, *in situ* compression tests were performed in the tomograph. The images of the deformed sample show a progressive buckling of the vertical struts leading to final fracture. The deformation initiated where the defects were present in the strut i.e. in regions with reduced local thickness. The finite element modelling confirmed the high stress concentrations of these weak points leading to the fracture of the sample.

## Highlights

- CoCrMo samples fabricated by Electron Beam Melting (EBM) process are considered.
- X-ray Computed Tomography is used to observe the structure of the sample.
- The mechanical properties are tested thanks to an *in situ* test in the tomograph.
- A Finite element model is developed to model the mechanical behaviour.

## 1. Introduction

For many years, cobalt-chromium-molybdenum CoCrMo alloys have been used as biomedical devices, e.g. for orthopaedic prostheses or dental implants, due to an interesting combination of properties: biocompatibility, high strength and hardness, and good corrosion resistance. Various studies have been performed on the relationship between microstructure and mechanical properties of the biomedical Co<sub>29</sub>Cr<sub>6</sub>Mo alloy [1, 2, 3, 4, 5]. Dense metallic implants have been extensively used but they have some drawbacks: a high density and mechanical properties that do not match with that of bone. For example, Co-Cr-Mo alloys have a Young's modulus of 230 GPa while the value for bone is 15 GPa. This difference of stiffness creates a phenomenon called stress shielding, which

causes bone resorption around the implant and reduces the life span of the device. Development of porous implants have been proved to be a solution to overcome these problems [6]. The porosity enables to lower the mechanical properties towards those of bone. The bone in-growth around the implants is also improved by colonization of pores by living cells. Conventional fabrication processes failed in providing porous samples with complex shape, desired porosity and mechanical properties. Producing such samples from casting of liquid alloy would lead different defects such as residual pores or other heterogeneities. For these reasons, Additive Manufacturing (AM) techniques have been developed to create innovative samples with desired porosity and shape [6]. For metals, Selective Laser Melting (SLM) and Electron Beam Melting (EBM) are currently the most popular techniques. Different authors fabricated biomedical devices with these processes with titanium alloys [7, 8, 9, 10, 11, 12, 13] and also with the above mentioned biomedical cobalt-based alloy [14, 15, 16, 17]. However, this also creates new specific defects that can have detrimental effects on mechanical properties. The aim of this paper is to characterize the structural and mechanical properties of CoCrMo samples produced by EBM. For this purpose, samples were characterized thanks to X-Ray Computed Tomography (XRCT). This technique has become the most popular means of characterization of highly porous materials because it is non-destructive and enables to provide three dimensional information about the cellular samples with no special sample preparation [18]. Typical resolutions of few microns are used to observe the mesoscopic architecture of the samples. But, it is also possible to obtain information about the fine scale microstructural features of the solid phase thanks to the so-called local tomography mode [19]. In this mode, the sample is placed near the X-ray source and a high resolution image of the irradiated part of the specimen is obtained. The samples were compressed *in situ* in XRCT to obtain images at different levels of strain. Finally, a Finite Element (FE) model was built from the tomographic images at low resolution. The tomographic images at two resolutions, the *in situ* test and the FE calculations were combined to explain the mechanical behaviour of the material.

## 2. Material and methods

### 2.1. Fabrication of the materials

We prepared the samples according to the process described in the paper published by Sun *et al.* [20]. The cobalt powder used in the experiment had the composition given in table 1 and was made of spherical particles with an average particle size of 64  $\mu\text{m}$ . It has to be noted that the powder composition is in the range of the ASTM F75 standard. The samples were fabricated with a special device (*Arcam AB, Mölndal, Sweden*). An electron beam was focused thanks to electromagnetic lenses and sent to a layer of powder. The powder was raked on the substrate from a powder stock. A first beam scan pre-heated the powder at a temperature of 840°C and the powder was selectively melted at a temperature of 1430°C (i.e. the melting point of the cobalt-based alloy). A new layer was then subsequently created onto the previous layers already built which formed the sample under construction. The powder is selectively melted according to a model previously generated by a Computer Aided Design (CAD) software. The samples had a cubic shape with a dimension of 20 mm. The cells were targeted to have a size of 1.2 mm and wall size of 400  $\mu\text{m}$ . The direction 3 is referred as the building direction. After fabrication, the samples underwent an ageing heat treatment at 800°C during 24 hours to transform the  $\gamma$  (fcc) phase into  $\epsilon$  (hcp) phase. In a previous paper, microstructural analysis evidenced that the grains were fully transformed into the single  $\epsilon$  phase by the ageing treatment [20]. Precipitates such as  $\text{M}_2\text{N}$  nitrides and  $\text{M}_{23}\text{C}_6$  carbides were also identified with M being Cr, Mo and Si.

A small sample with dimensions of 4.6 x 4.7 x 3.9 mm<sup>3</sup> (respectively directions 1, 2 and 3) was cut from one of the larger samples with a micro-saw (*IsoMet 1000, Buehler, Germany*). These dimensions were chosen to have a sample small enough to be inserted into the *in situ* mechanical test device.

The geometric relative density was calculated from the weight and the dimensions of the large samples, considering a density of  $8.4 \text{ g.cm}^{-3}$  for the fully dense CoCrMo alloy.

The sample was observed thanks to Scanning Electron Microscope (SEM, *SUPRA VP55, Zeiss, Germany*) at a voltage of 10 kV.

Nanoindentation was used to determine the mechanical properties of the solid phase of the sample. For this purpose, a sample was embedded in a plastic resin and carefully polished down to  $1 \mu\text{m}$  with diamond paste. The nanoindentation system (*Agilent G200, Agilent Technologies, USA*) was equipped with a Berkovich tip. Due to the geometry of the Berkovich tip, the indent length is equal to seven times the indent depth. The applied load was chosen so that the indent was fully localized in the solid wall. A series of 10 indents was made with a speed of  $10 \text{ nm.s}^{-1}$  and dwell time of 10 s. The calculation of Young's modulus from nanoindentation experiments was done through the use of the continuous stiffness measurement mode (CSM).

## 2.2. X-ray tomography

A laboratory X-ray tomograph (*Phoenix vTomeX / X ray, Germany*) described in [21] was used to scan the sample. Due to the high absorption coefficient of the cobalt-based alloys, the tomograph was operated at 100 kV and  $140 \mu\text{A}$  with a 0.3 mm copper filter on the incident X-rays. The whole sample was scanned at a resolution of  $15 \mu\text{m}$  (i.e. voxel size of  $15 \mu\text{m}$ ). The source to detector is fixed to 80 cm in our device. To obtain low resolution, the distance between the X-ray source and the sample was 10 cm. In this configuration, the whole sample was irradiated by the X-ray conical beam. In order to observe the finer details of the microstructure, local tomography was subsequently used [21]. In this mode, only a part of the sample was irradiated by X-rays under all the viewing angles as the field of view of the detector was smaller than the size of the sample. A part of the sample is not seen by the detector for some angles of rotation. But, some authors demonstrated that it is possible to reconstruct a 3D image without noise [22, 23]. For this purpose, the sample was placed very close to the X-ray

source: the distance between the source and the sample was then only 1 cm. Using this mode, a high resolution reconstruction of the irradiated part of the sample could be obtained with a voxel size of 3  $\mu\text{m}$ . To scan another part of the sample, it was then sufficient to physically displace the specimen on the rotating stage. Reconstructing the whole volume of the sample at high resolution required that we acquired 8 images, each representing a part of the sample.

A home-made compression rig was inserted in the tomograph to perform the compression test as described in [19]. The sample was placed between two grips acting as compression platens. The upper platen was screwed to a force sensor. The set (force sensor, platens and sample) was placed into an aluminium tube with an inner diameter of 16 mm and a thickness of 4 mm. The latter was then screwed to the motor. Aluminium has a mass attenuation coefficient of  $0.37 \text{ cm}^2/\text{g}$  for a beam with a voltage of 100 kV [24]. This value is lower than that of cobalt ( $2.14 \text{ cm}^2/\text{g}$ ). Therefore, the presence of the aluminium tube does not impeach scanning of the sample during the *in situ* test. The displacement was applied by the motor via a home-made software with a speed of  $0.01 \text{ mm.s}^{-1}$ . The reaction force was measured by the force sensor and recorded by a second home-made software. The test was interrupted to scan the sample at different strains with the voxel size of 20  $\mu\text{m}$ . The difference of length between images of initial and deformed states was used to calculate average strain.

### 2.3. Image processing and analysis

Image processing of the 3D images was performed using the ImageJ software. The low resolution image of the initial sample was processed to improve the image quality: adjustment of contrast and brightness, application of median filtering over neighbours of two voxels. Then, it was thresholded to separate the pores from the solid phase.

The thresholded image was used to perform different morphological characterizations. A more

detailed description of these measurements is explained in [25].

The relative density was determined as the ratio of total voxels belonging to the solid phase compared to the total number of voxels.

The distributions of the pore size and of the cell wall thickness were measured by a technique of granulometry comparable to sieving of a powder. It consists in applying a series of erosion and dilation operations to the studied phase of the image. A histogram giving the pore size or the cell wall thickness distribution is obtained.

#### *2.4. FE modelling*

The low resolution 3D image of the initial sample was meshed with 1200000 quadratic tetrahedra having an edge size of 54  $\mu\text{m}$  by Avizo 8 software. A negative displacement corresponding to the strain reached during the mechanical test was applied to the top nodes in the direction 3 whereas the nodes of the opposite faces were displacement constrained. An elastoplastic behaviour was assumed for the CoCrMo material. A Young's modulus of 230 GPa (determined by nanoindentation) and a Poisson's ratio of 0.3 were considered for elastic properties. This value of Young's modulus is close to one determined in literature [26, 27]. Plastic stresses and strains were defined following the compression stress/strain curve from Montero-Ocampo *et al.* [28]. This curve was obtained for a CoCrMo alloy (having a chemical composition in accordance with the ASTM F75 standard) cast at a temperature of 1430°C (melting temperature of the alloy) and heat treated at 815°C during 24 hours. The melting of powder during EBM is certainly a different process from the casting of liquid alloy. Therefore, the compression stress/strain of a dense CoCrMo alloy made by EBM would certainly not have exactly this profile. But, without existing data about a uniaxial compression test of dense samples made by EBM, it was necessary to choose data from alloys made by casting.



### 3. Results

#### *3.1. Qualitative and quantitative description of the sample*

The periodic square cell structure is visible thanks to 3D visualization (fig. 1a) and a SEM image of the sample (fig. 1b). The 3D visualization was built from low resolution tomographic image with a voxel size of 15  $\mu\text{m}$ . The sample has an apparent density of 0.24. The relative density calculated by ImageJ is 0.25 in good agreement with the previous value. The relative density distribution (fig. 2) shows alternation of dense slices and more porous ones. The direction 3 corresponds to the building axis during the EBM process. Each curve is periodic which is consistent with the cubic pore structure (fig. 2).

The low resolution image (fig. 3a) enables to notice the important roughness at the surface of the sample in all the struts. Some pores are also visible in the solid phase. This is confirmed by images obtained thanks to local tomography. The high resolution images revealed the presence of many morphological defects in the solid struts. We present hereafter tomographic images (3D visualization and slices) of some zones in the sample. First, different pores with various shapes are noticed in the struts (see fig. 3a showing a horizontal strut). In fig. 4a, sets of small solid spheres are visible in the solid phase (see the red ellipse). They give a rough aspect to the surface (visible in 3D image in fig. 4a). The spheres are partially melted particles which attached to the sample during the process. Fig. 3b shows a strut where no attached particles are present. Its surface has an important roughness which is the cause of irregular thickness along the struts (see the vertical struts in 3D in fig. 3b and in 2D in fig. 4b). These defects are not visible in lower resolution images and are revealed by local tomography. The interest of local tomography lies in the possibility to scan the whole sample at high resolution and to characterize completely the presence of defects.

The strut thickness and cell size distributions obtained from 3D granulometry on tomographic volume are shown in fig. 5a and 5b. The structural element used to measure the granulometric distribution was a sphere. The strut thickness distribution from tomographic image is rather wide around the main peak. This is consistent with the presence of defects seen on fig. 3 and 4. The pore size distribution possesses a main peak corresponding to the macro-pores with a square cross-section and a smaller peak around 120  $\mu\text{m}$ , indicating the presence of smaller pores. The wide size distributions of solid and porous phases illustrate the presence of heterogeneities in the structure.

### *3.2. In situ compression test*

Fig. 6 presents the compression engineering stress versus engineering strain curve. The stress/strain curve presents a first elastic domain followed by a plastic part. The low ductility of the CoCrMo alloy is an explanation of the brittle failure of the struts and of the absence of stress plateau and densification regions.

The mechanical properties obtained from the compression test for this sample and for a second one are summarized in table 2, as well as some data extracted from literature on compression of CoCrMo cellular samples. The quoted authors of the table studied CoCrMo cubic lattice structures made by AM (EBM or SLM) in compression. Our results are in relatively good agreement with these previous experiments. The ratio of the cell over the sample size has already been shown to have an influence on the mechanical properties, with a smaller strength for samples with fewer cells [29]. The quoted authors tested samples with 6 cells in each direction whereas our sample has only 2 cells in each direction. This can explain their higher relative yield strength and relative compression strength. Moreover, the difference obtained by the two quoted authors can be explained by the different processes used (i.e. EBM) and the different relative densities achieved.

Fig. 7 shows a 3D visualization of some struts of the sample during the *in situ* compression test. Deformation localizes in the upper struts and especially in the left one. Buckling is visible in this strut at a strain of 2.5% (see fig. 7b). This strain corresponds to the macroscopic linear elastic part of the stress/strain curve (see fig. 6). The deformation visible in the images could be caused by local micro-plasticity. With increasing strain, stress exceeded yield point. At this stage (i.e. strain of 4.7% shown in fig. 7c), the deformation in the upper struts increases. This localization of deformation in some struts created a deformation band perpendicular to the loading direction typical of a cellular material tested in compression. This corresponds in the stress/strain curve to the beginning of the stress plateau. But, the vertical struts progressively broke leading to a decrease of stress until separation of the sample into two parts. This is not shown in the figure. Fig. 7c also shows the deformation localizes in a part of the strut (see the red frame). The corresponding high resolution image of this strut (fig. 7d) evidences the presence of an agglomerate of partially melted particles at the exact location of the deformation.

### 3.3. FE modelling

Fig. 8 presents the experimental and the modelled stress/strain curve. The calculated Young's modulus was ten times higher than the experimental one. This has already been observed for finite element modelling of cellular samples [32]. No clear explanation exists about this overestimation [33]. On the contrary, there was a good agreement between experiment and modelling for the plastic part of the curve (between the yield point and the compression strength).

The normal  $\sigma_{33}$  stress distributions for the struts (at a strain of 4.7 %) are shown in fig. 9. It is seen that the finite element model predicts higher stress in the upper struts. The defects due to fabrication such as reduced thickness in the struts concentrate the stresses as it is visible in fig. 9. This confirms the experimental findings about the detrimental influence of these specific defects.

#### 4. Discussion

CoCrMo cellular samples exhibit a mechanical behaviour which has already been observed by other authors for cubic unit cell structures [30, 34]. The deformation occurs by buckling of vertical struts followed by a layer by layer collapse of the sample [35].

The plastic deformation initiates in weak zones where some defects are present. These defects are difficult to observe with low resolution image of the whole sample and are revealed by local tomography. These defects are caused by the EBM process: small pores in the solid phase, attached particles in the surface, irregular thickness along the strut. Other authors have already noticed the presence of defects in samples made by EBM or SLM. Murr *et al.* [16] or Pupo *et al.* [36] found the important role of roughness in CoCrMo structures made by SLM. The presence of partially melted particles on the surface has already been observed by SEM by Yan *et al.* with stainless steel samples made by SLM [13]. But, up to now, local tomography has not been used to scan a whole sample at high resolution. The scans performed in this study enable to observe the presence of the defects in all the sample and to link them to the zones of deformation during the compression. This is confirmed by the FE calculation which predicts that the defects constitute weak points in the structure.

This new information should encourage the use of local tomography to better characterize the structure of the EBM- or SLM-built samples. They also prove that improvements of these AM processes are necessary to remove these defects which are caused by a non-optimized process. The presence of spherical residual pores can be linked to entrapment of gas in the powder in the EBM build chamber. The gas bubbles could not escape during melting of powder and generated pores. More irregularly shaped pores are linked to an incomplete melting of powder during the process [37]. The presence of attached particles is caused by a partial melting of some powder particles during the EBM.

Different parameters of the process can be optimized: powder characteristics, scanning parameters, electron beam or laser beam parameters. Post-processing operations can also be done: Yan *et al.* [13] propose to sand-blast the samples after EBM to remove the particles, Pattanayak *et al.* [38] heat treat their samples to fuse the particles and to bond them to the surface.

## 5. Conclusion

The EBM manufacturing technique was successfully used to produce porous samples with cubic unit cells. X-ray computed tomography is useful to characterize quantitatively and qualitatively the architecture of the samples. Local tomography revealed the presence of different defects due to the fabrication process, especially at the strut surface: pores in the solid phase, partially melted particles attached to the surface giving a rough aspect to the surface, irregular thickness along the struts. *In situ* compression test performed on this sample showed a typical cellular behaviour with deformation followed by fracture of the upper struts by buckling. Careful examination of the tomographic volumes showed an influence of the fabrication defects on the initiation of the deformation. The presence of thinner zones surrounded by bump of partially melted particles constituted weak points of the sample which initiated the buckling. Consequently, the FE calculation predicted the highest stresses in the zones of reduced thickness and of partially melted particles in the vertical struts.

## 6. Acknowledgements

The authors acknowledge José Ferreira (MATEIS laboratory, INSA Lyon) who developed the softwares used for the *in situ* mechanical test.

## 7. References

- [1] L.E. Ramírez, M. Castro, M. Méndez, J. Lacaze, M. Herrera, G. Lesoult, Precipitation path of secondary phases during solidification of the Co-25.5%Cr-5.5%Mo-0.26%C alloy, *Scripta Mater.* 47 (2002) 811-816, 2002.
- [2] M. Herrera, A. Espinoza, J. Mendez, M. Castro, J. Lopez, J. Rendon, Effect of C content on the mechanical properties of solution treated as-cast ASTM F-75 alloys, *J. Mater. Sci. - Mater. Med.* 16 (2005) 607-611.
- [3] S.H. Lee, N. Nomura, A. Chiba, Effect of Fe addition on microstructures and mechanical properties of Ni- and C-Free Co-Cr-Mo alloys, *Mater. Trans.* 48 (2007) 2207-2211.
- [4] J.V. Giacchi, O. Fornaro, H. Palacio, Microstructural evolution during solution treatment of Co-Cr-Mo-C biocompatible alloys, *Mater. Charact.* 68 (2012) 49-57.
- [5] M. Podrez-Radziszewska, K. Haimann, W. Dudziński, M. Morawska-Sołtysik, Characteristic of intermetallic phases in cast dental CoCrMo alloy, *Arch. Foundry Eng.* 10 (2010) 51-56.
- [6] L.E. Murr, S.M. Gaytan, E. Martinez, E. Martinez, F. Medina, R.B. Wicker, Next generation orthopaedic implants by additive manufacturing using electron beam melting, *Int. J. Biomater.* 2012 (2012) 1-14.
- [7] D.A. Hollander, M. Von Walter, T. Wirtz, R. Sellei, B. Schmidt-Rohlfing, O. Paar, H.-J. Erli, Structural, mechanical and in vitro characterization of individually structured Ti-6Al-4V produced by direct laser forming, *Biomaterials* 27 (2006) 955-963.
- [8] G.E. Ryan, A.S. Pandit, D.P. Apatsidis, Porous titanium scaffolds fabricated using a rapid prototyping and powder metallurgy technique, *Biomaterials* 29 (2008) 3625-3635.
- [9] M.A. Lopez-Heredia, E. Goyenvalle, E. Aguado, P. Pilet, C. Leroux, M. Dorget, P. Weiss, P. Layrolle, Bone growth in rapid prototyped porous titanium implants, *J. Biomed. Mater. Res. A* 85 (2008) 664-673.

- [10] B. Gorny, T. Niendorf, J. Lackmann, M. Thoene, T. Troester, H.J. Maier, *In situ* characterization of the deformation and failure behaviour of non-stochastic porous structures processed by selective laser melting, *Mater. Sci. Eng. A* 528 (2011) 7962-7967.
- [11] J. Wieding, A. Jonitz, R. Bader, The effect of structural design on mechanical properties and cellular response of additive manufactured titanium scaffolds, *Materials* 5 (2012) 1336-1347.
- [12] S. Ponader, C. Von Wilmowsky, M. Widenmayer, R. Lutz, P. Heintl, C. Körner, R.F. Singer, E. Nkenke, F.W. Neukam, K.A. Schlegel, *In vivo* performance of selective electron beam-melted Ti-6Al-4V structures, *J. Biomed. Mater. Res. A* 92 (2010) 56-62.
- [13] C. Yan, L. Hao, A. Hussein, D. Raymont, Evaluations of cellular lattice structures manufactured using selective laser melting, *Int. J. Mach. Tools Manuf.* 62 (2012) 32-38.
- [14] S.M. Gaytan, L.E. Murr, E. Martinez, J.L. Martinez, B.I. Machado, D.A. Ramirez, F. Medina, S. Collins, R.B. Wicker, Comparison of microstructures and mechanical properties for solid and mesh cobalt-base alloy prototypes fabricated by Electron Beam Melting, *Metall. Mater. Trans. A* 41 (2010) 3216- 3227.
- [15] S.M. Gaytan, L.E. Murr, D.A. Ramirez, B. I. Machado, E. Martinez, D.H. Hernandez, J.L. Martinez, F. Medina, R.B. Wick, A TEM study of cobalt-based alloy prototypes fabricated by EBM, *Mater. Sci. App.* 2 (2011) 355-363.
- [16] L.E. Murr, K.N. Amato, S.J. Li, Y.X. Tian, X.Y. Cheng, S.M. Gaytan, E. Martinez, P.W. Shindo, F. Medina, R.B. Wicker, Microstructure and mechanical properties of open-cellular biomaterials prototypes for total knee replacement implants fabricated by electron beam melting, *J. Mech. Behav. Biomed. Mater.* 4 (2011) 1396-1411.
- [17] S. Rivera, M. Panera, D. Miranda, F.J. Belzunce Varela, Development of dense and cellular solids CrCoMo alloy for orthopaedic applications. *Proc. Eng.* 10 (2011) 2979-2987.
- [18] E. Maire, X-Ray tomography applied to the characterization of highly porous materials, *Annu. Rev. Mater. Res.* 42 (2012) 7.1-7.16.

- [19] T. Zhang, E. Maire, J. Adrien, P.R. Onck, L. Salvo, Local tomography study of the fracture of an ERG metal foam, *Adv. Eng. Mater.* 15 (2013) 762-772.
- [20] S.-H. Sun, Y. Koizumi, S. Kurosu, Y.-P. Li, H. Matsumoto, A. Chiba, Build direction dependence of microstructure and high-temperature tensile property of Co-Cr-Mo alloy fabricated by electron beam melting, *Acta Mater.* 64 (2014) 154-168.
- [21] J.-Y. Buffière, E. Maire, J. Adrien, J.-P. Masse, E. Boller, *In situ* experiments with X ray tomography: an attractive tool for experimental mechanics, *Exp. Mech.* 50 (2010) 289-305.
- [22] S. Youssef, E. Maire, R. Gaertner, Finite element modelling of the actual structure of cellular materials determined by X-ray tomography, *Acta Mater.* 53 (2005) 719-730.
- [23] H. Toda, T. Ohgaki, K. Uesugi, M. Kobayashi, N. Kuroda, T. Kobayashi, M. Niinomi, T. Akahori, K. Makii, Y. Aruga, Quantitative assessment of microstructure and its effects on compression behavior of aluminum foams via high-resolution synchrotron X-ray tomography, *Metall. Mater. Trans.* 37A (2006) 1211-1219.
- [24] Hubbell, J.H. and Seltzer, S.M. (2004), Tables of X-Ray Mass Attenuation Coefficients and Mass Energy-Absorption Coefficients (version 1.4). [Online] Available: <http://physics.nist.gov/xaamdi> [2016]. National Institute of Standards and Technology, Gaithersburg, MD.
- [25] E. Maire, P. Colombo, J. Adrien, L. Babout, L. Biasetto, Characterization of the morphology of cellular ceramics by 3D image processing of X-ray tomography, *J. Eur. Ceram. Soc.* 27 (2007) 1973-1981.
- [26] C. Balagna, M.G. Faga, S. Spriano, Tantalum-based multilayer coating on cobalt alloys in total hip and knee replacement, *Mater. Sci. Eng. C* 32 (2012) 887-895.
- [27] J.A. Ortega-Saenza, M.A.L. Hernandez-Rodrigueza, V. Ventura-Sobrevilla, R. Michalczewski, J. Smolik, M. Szczerek, Tribological and corrosion testing of surface engineered surgical grade CoCrMo alloy, *Wear* 271 (2011) 2125-2131.
- [28] C. Montero-Ocampo, M. Talavera, H. Lopez, Effect of alloy preheating on the mechanical



properties of as-cast Co-Cr-Mo-C alloys, *Metall. Mater. Trans. A* 30 (1999) 611-620.

[29] E. Andrews, G. Gioux, P.R. Onck, L.J. Gibson, Size effects in ductile cellular solids. Part II: experimental results, *Int. J. Mech. Sci.* 43 (2001) 701-713.

[30] K. Hazlehurst, C.J. Wang, M. Stanford, Evaluation of the stiffness characteristics of square pore CoCrMo cellular structures manufactured by laser melting technology for potential orthopaedic applications, *Mater. Des.* 51 (2013) 949-955.

[31] S.A. Che Ghani, N.M.S.N. Malek, W.S. Wan Harun, Z. Adnan, F.F. Rashid, M.H. Ramli, M.A. Omar, Finite element analysis of porous medical grade cobalt chromium alloy structures produced by selective laser melting. 2015. Available on:

< [http://www.academia.edu/10213281/Finite\\_element\\_analysis\\_of\\_porous\\_medical\\_grade\\_cobalt\\_chromium\\_alloy\\_structures\\_produced\\_by\\_selective\\_laser\\_melting](http://www.academia.edu/10213281/Finite_element_analysis_of_porous_medical_grade_cobalt_chromium_alloy_structures_produced_by_selective_laser_melting) >

[32] O. Caty, E. Maire, S. Youssef, R. Bouchet, Modelling the properties of closed-cell cellular materials from tomography images using finite shell elements, *Acta Mater.* 56 (2008) 5524-5534.

[33] C. Petit, S. Meille, E. Maire, Cellular solids studied by X-ray tomography and finite element modeling - a review, *J. Mater. Res.* 28 (2013) 2191-2201.

[34] J. Kadkhodapour, H. Montazerian, A.C. Darabi, A.P. Anaraki, S.M. Ahmadi, A.A. Zadpoor, S. Schmauder, Failure mechanisms of additively manufactured porous biomaterials: Effects of porosity and type of unit cell, *J. Mech. Behav. Biomed. Mater.* 50 (2015) 180-191.

[35] S.M. Ahmadi, S.A. Yavari, R. Wauthle, B. Pouran, J. Schrooten, H. Weinans, A.A. Zadpoor, Additively manufactured open-cell porous biomaterials made from six different space-filling unit cells: the mechanical and morphological properties, *Materials* 8 (2015) 1871-1896.

[36] Y. Pupo, L. Sereno, J. De Ciurana, Surface quality analysis in Selective Laser Melting with CoCrMo powders, *Mater. Sci. Forum* 797 (2014) 157-162.

[37] S. Tammis-Williams, H. Zhao, F. Leonard, F. Derguti, I. Todd, P.B. Prangnell, XCT analysis of the influence of melt strategies on defect population in Ti-6Al-4V components manufactured by

Selective Electron Beam Melting, Mater. Charact. 102 (2015) 47-61.

[38] D.K. Pattanayak, A. Fukuda, T. Matsushita, M. Takemoto, S. Fujibayashi, K. Sasaki, N. Nishida, T. Nakamura, T. Kokubo, Bioactive Ti metal analogous to human cancellous bone: fabrication by selective laser melting, Acta Biomater. 7 (2011) 1398-1406.

## Figures and tables

Table 1: Chemical composition of the CoCrMo powder used for fabrication (wt. %) [20]

Table 2: Young's modulus, yield strength and compression strength obtained from the compression test in this study and comparison with values from the literature for other CoCrMo cellular samples

Fig. 1: Compression stress/strain curve of a biomedical CoCrMo alloy used in the model [24]

Fig. 2: (a) 3D image of the whole sample and (b) relative density profile along the three directions

Fig. 3: 3D images of some struts showing: (a) the globular aspect of the surface and (b) the irregular thickness

Fig. 4: Slices from tomographic images showing: (a) top view of a part of the sample and (b) cross sections of a strut

Fig. 5: (a) Strut size and (b) pore size distribution of the sample measured by image processing granulometry [22] using a spherical structural element

Fig. 6: Experimental compression stress/strain of the sample

Fig. 7: 3D visualization of the sample with tomographic images with a voxel size of 15  $\mu\text{m}$ : (a) initial state, (b) at a strain of 1.4 %, (c) at a strain of 2.5 % and (d) at a strain of 4.7 %

Fig. 8: Experimental and simulated stress/strain curves

Fig. 9: Result of the simulation for some struts at a strain of 4.7 %

Table 1

Co	Cr	Mo	Ni	Si	Mn	C	N	O
63.2	28.4	6.66	0.18	0.45	0.69	0.23	0.2	0.023

Table 2

Reference	Fabrication/Unit lattice	Relative density	Young's modulus (GPa)	Yield strength (MPa)	Compression strength (MPa)
This study Our sample	EBM/Cube	0.25	$4.9 \pm 1.1$	45.6	64.3
Examples of other samples from the literature					
Hazlehurst et al. [30]	SLM/Cube	0.18	$4.8 \pm 0.5$	$65.4 \pm 1.8$	90
Che Ghani et al. [31]	EBM/Cube	0.2	3.8	49	57.4

Fig. 1

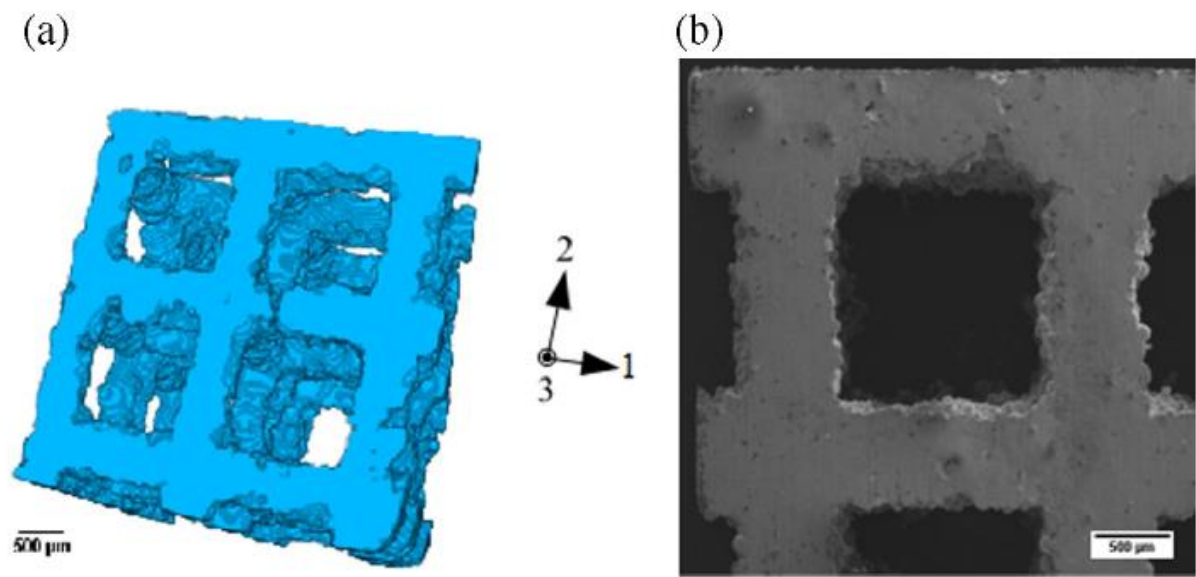


Fig 2

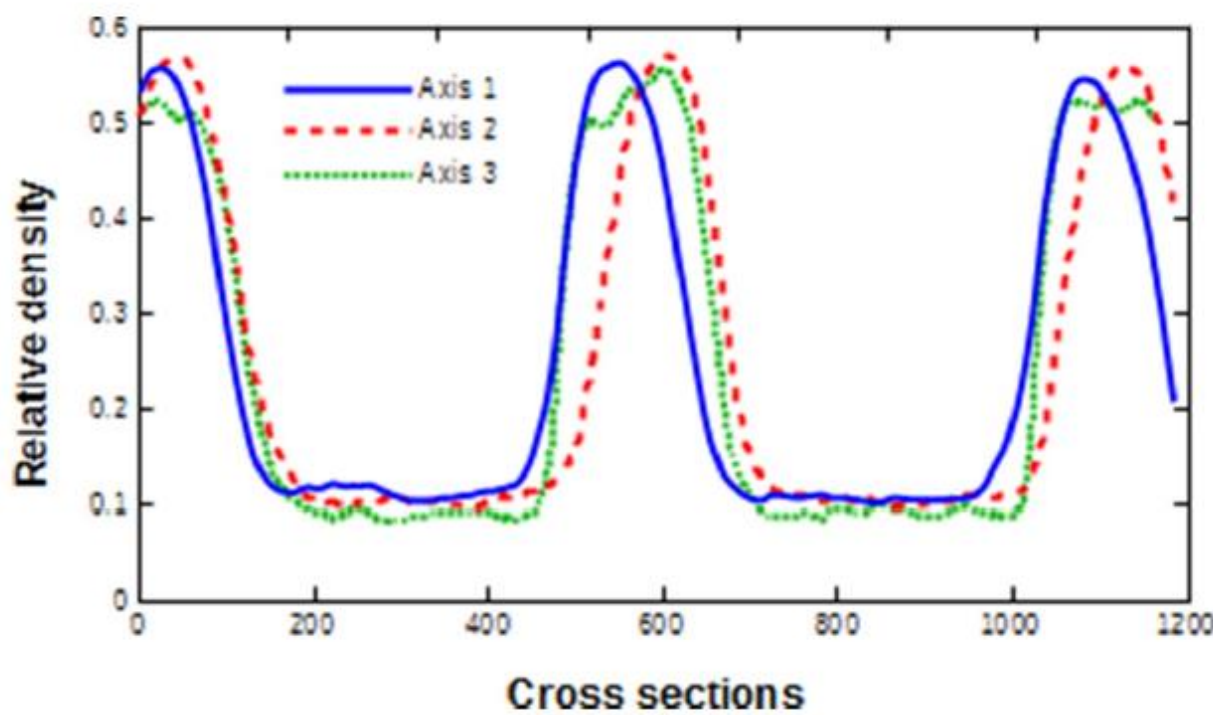


Fig 3

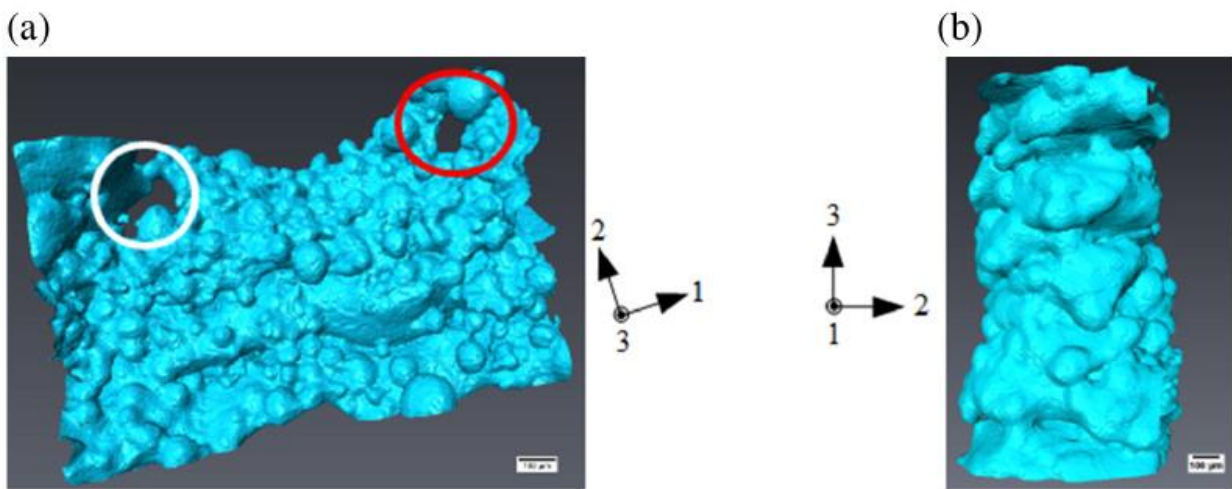


Fig 4

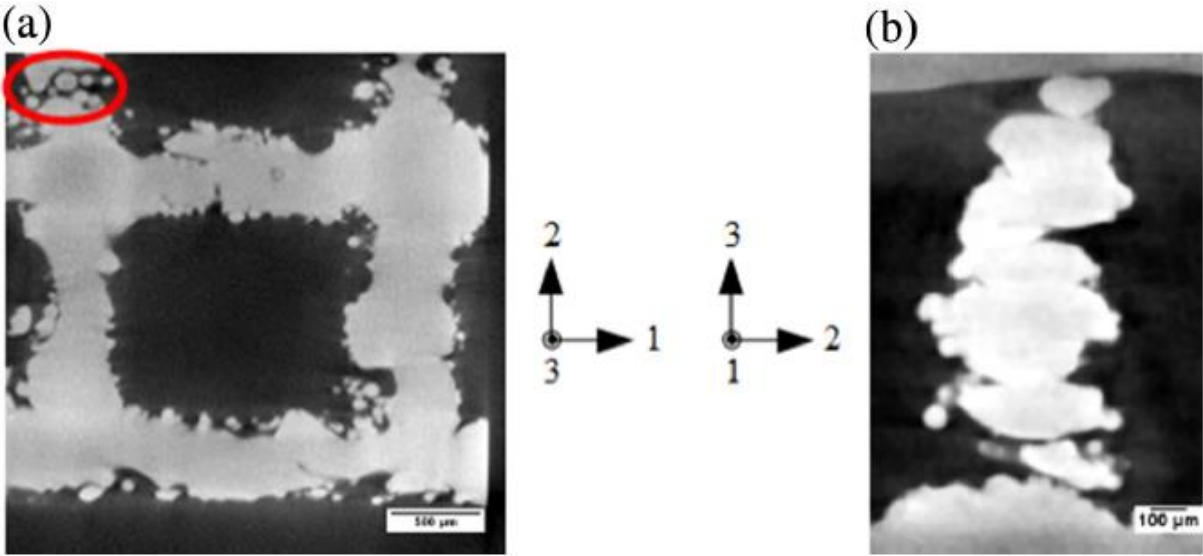


Fig 5

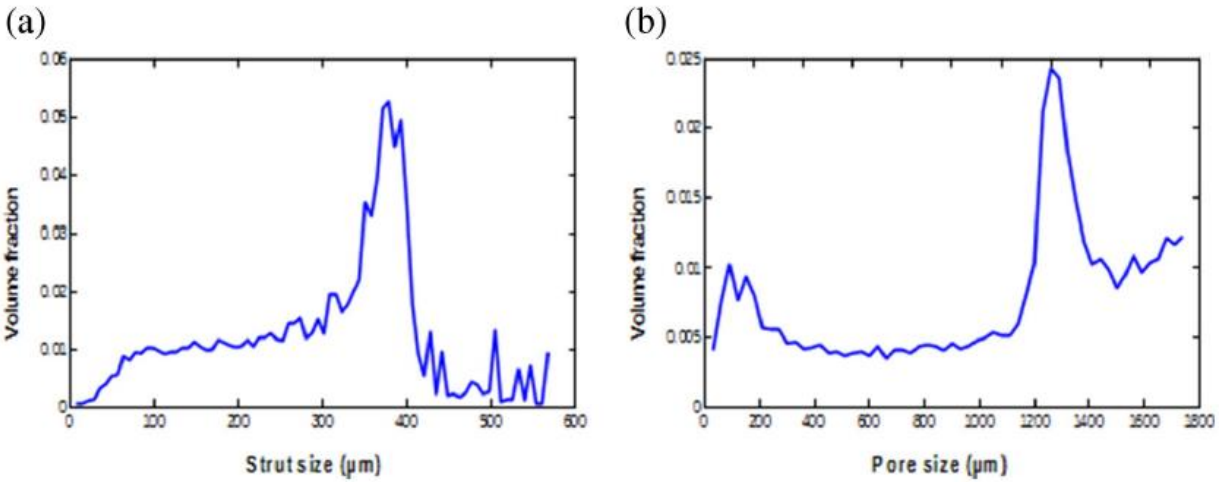


Fig 6

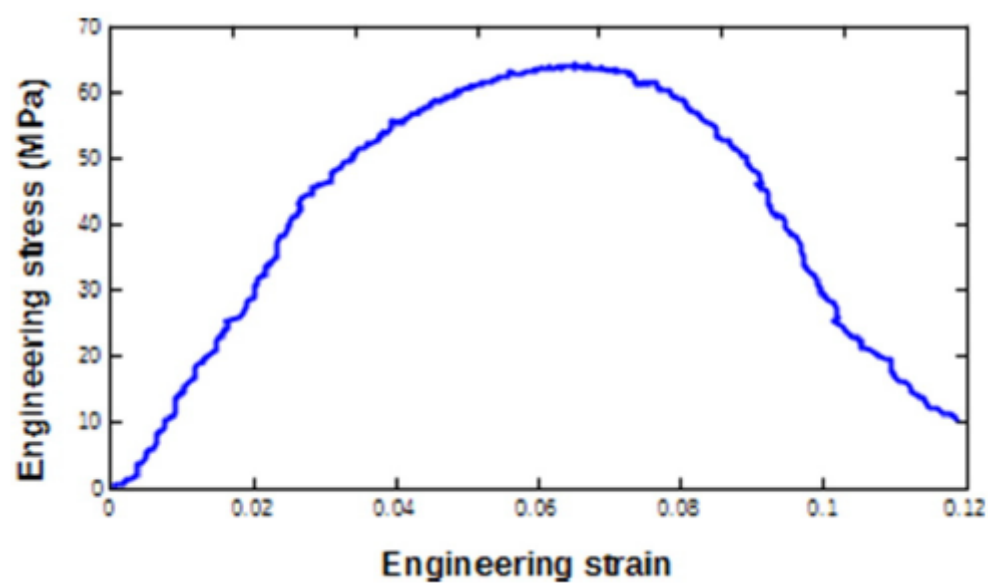


Fig 7

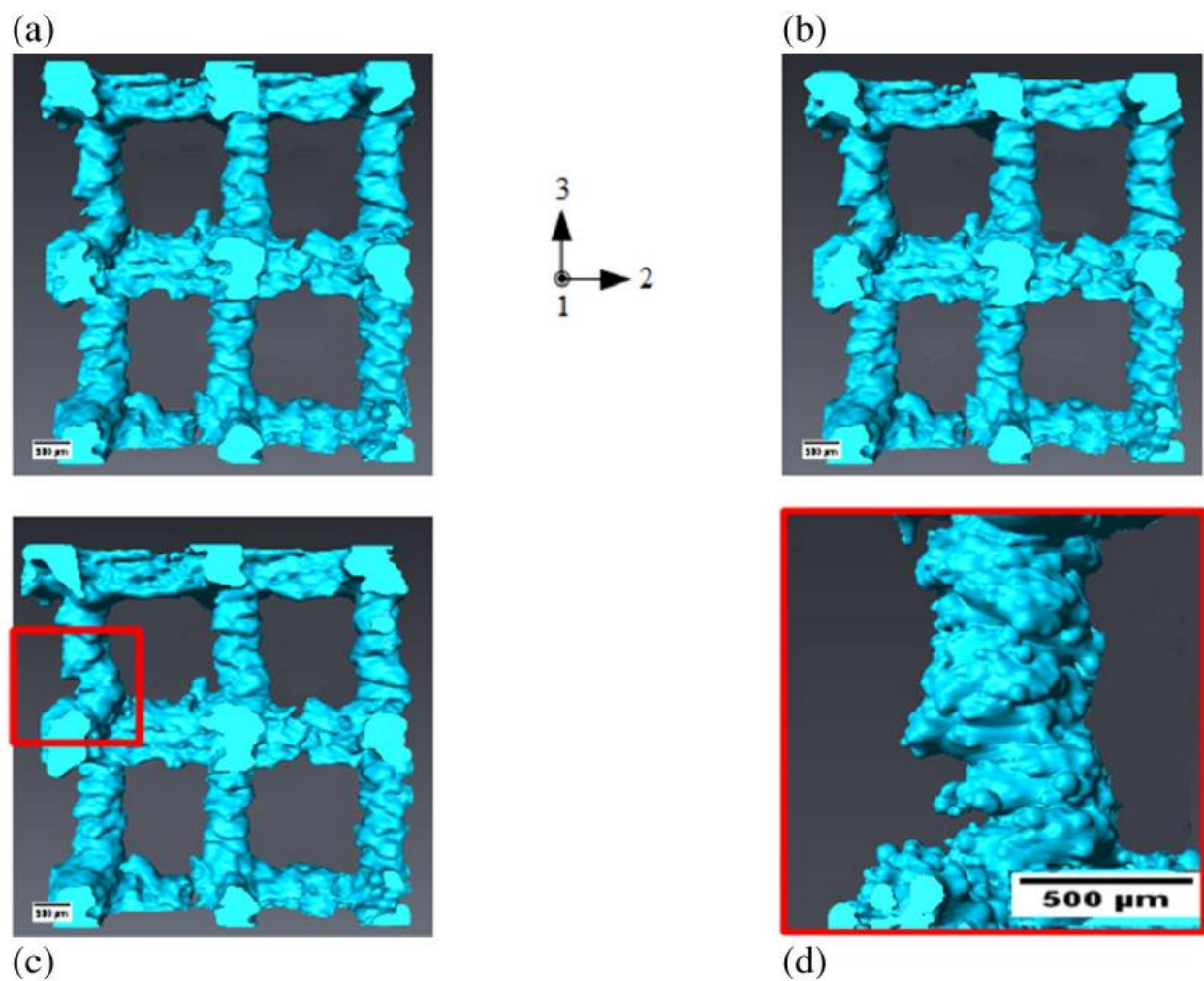


Fig 8

